B.Y. Zhou, M. Morelli, N.R. Gauger, A. Guardone
Simulation and Sensitivity Analysis of a Wing-Tip Mounted Propeller Configuration from the Workshop for Integrated Propeller Prediction (WIPP)
in: AIAA Aviation Forum 2020, AIAA, 2020, ISBN: 9781624105982, p. 1-22, AIAA 2020-2683
[AIAA Aviation Forum 2020, Reno, NV, USA, 15-19 June 2020]
doi:10.2514/6.2020-2683

Simulation and Sensitivity Analysis of a Wing-Tip Mounted Propeller Configuration from the Workshop for Integrated Propeller Prediction (WIPP)

Beckett Y. Zhou* and Nicolas R. Gauger †

Chair for Scientific Computing, TU Kaiserslautern

Bldg 34, Paul-Ehrlich-Strasse, 67663 Kaiserslautern, Germany

Myles Morelli ‡ and Alberto Guardone§

Department of Aerospace Science and Technology, Politecnico di Milano

Building B12, Via La Masa 34, Milano, MI 20156, Italy

In this work, the turbulent flow field around a wing-tip mounted propeller configuration is simulated using the model and test conditions released by the Workshop for Integrated Propeller Prediction (WIPP). In particular, the unsteady Reynolds-averaged Navier-Stokes and enhanced delayed detached eddy simulations with Spalart-Allmaras turbulence model are performed in a time-accurate manner with the multi-zone sliding mesh technique in which the propeller is allowed to rotate while the wing and the nacelle remain stationary. Time-averaged pressure coefficients at six spanwise locations along the wing surface are shown to be in good agreement with the experimental data, including the two locations directly in the propeller slipstream. Numerical predictions on finer grids are found to capture the general shapes of the wake profiles well compared with experimental data from the wake survey, but the peak values are under-predicted on all wake profiles except for the swirl velocity. Moreover, there appears to be a shift radially inward indicating that the wake quantities, and the thrust in particular, do not extend beyond the propeller tip, as suggested by the experiment. The simulations on finer grids reveal two major noise sources of this wing-tip mounted propeller configuration, namely the turbulent wake and tip vortex generated by the propeller blades, both impinging upon the wing and nacelle surfaces as they convect downstream. Visualization of the surface pressure fluctuations reveals the noise footprints on this integrated propeller-wing system. In particular, the impingement of propeller blade tip vortices on the leading edge of the wing immediately below the nacelle is identified to be the dominant noise source. Making inroads into sensitivity analysis of the full propeller-wing assembly, an unsteady discrete adjoint approach based on algorithmic differentiation is applied to evaluate the surface sensitivity of an isolated WIPP propeller with respect to the mean thrust coefficient design objective.

I. Introduction

Propeller-driven engines have garnered renewed interest in the aircraft industry due to the emergence of electric and distributed propulsion systems. These systems, typically installed on lighter and slower vehicles, demand less engine power and attain lower blade tip speed, allowing them to achieve 10-20% higher fuel efficiency over typical turbofan engines in static and flight test conditions.[1] This inclination has led NASA to reinstate its X-Plane series, and with this, the latest aircraft under development is the experimental X-57 plane. Throughout the research and development of this aircraft, one of the key features is the use of wing-tip mounted propellers to increase the efficiency of the aircraft. A clean wing-tip produces strong three-dimensional vortical structures, so intuitively, the placement of propellers mounted on the wing-tips can help reduce the wings induced drag by attenuating the wing-tip vortex by the propeller

*Research Scientist, Member AIAA, yuxiang.zhou@scicomp.uni-kl.de

†Professor, Associate Fellow AIAA, nicolas.gauger@scicomp.uni-kl.de

‡PhD Candidate, Student Member AIAA, mylescarlo.morelli@polimi.it

§Professor, alberto.guardone@polimi.it

slipstream. In the past, a major drawback of wing-tip mounted propellers has been the integration of the propeller with the airframe and the issue of having a high mass at the wing tip causing aeroelastic problems. The emergence of electric and distributed propulsion systems however increases the design flexibility by eliminating potential penalties of down-scaling the motors.[2]

Wing-tip mounted propellers have a long and rich history due to their performance enhancements which have been well known for years on end. As early as 1969 Snyder[3] showed that wing-tip mounted tractor propellers could decrease wing drag and increase the wing's maximum lift if the propeller rotated in the opposite direction to that of the wing-tip vortex. Later the work of J. C. Patterson et al. in 1985 used wind tunnel experiments to study the effects of a wing-tip mounted pusher turboprop on the aerodynamic characteristics of a semi-span wing.[4] Their work suggested that large propulsive efficiency benefits and significant induced drag reductions could be achieved through the use of wing-tip mounted propellers. A year later in 1986, L. R. Miranda and J. E. Brennan began numerically investigating the benefits which could be achieved by properly mounting propellers at the wing-tips.[5] Their results confirmed the experimental wind tunnel test findings found the previous year and concluded that indeed significant aerodynamic performance improvements could be found from wing-tip mounted propellers. More recently in 2019, Sinnige et al.[6] noted that the present literature lacks comprehensive analyses of the aerodynamic interaction effects relevant of the wing-tip mounted propeller which are of crucial importance to fully exploit the configuration and harness the potential aerodynamic benefits. Their work used experimental PIV measurements downstream of the propeller and surface oil flows to to understand the interaction effects of the wing-tip mounted propeller. Moreover, it showed significant performance improvements when compared to a conventional configuration.

An undesirable factor associated with propeller-driven engines is their noise level. While the dominant noise source in such engines is due to the unsteady aerodynamic loading on the rotating propeller blades, various installation/integration noise sources have also been shown to be significant. These are typically known as the propeller-wing or propeller-fuselage interaction noise whereby the turbulent wake and tip vortices from the propeller blades impinge on the wing and the pylon transmitting unsteady aerodynamic loads leading to structure-borne cabin noise.[7] It is widely recognized that for certification of propeller-driven vehicles, aeroacoustic considerations must be the central focus of the design and no longer be treated a side constraint. Therefore accurate and robust numerical tools are urgently needed by the aircraft industry to characterize, predict and more importantly optimize novel propeller-powered configurations.

It is only until recently, however, that wing-tip mounted propellers are beginning to be seriously considered as viable configurations. To further understand wing-tip mounted propellers an open Workshop for Integrated Propeller Prediction (WIPP) has been established. The WIPP configuration provides experimental results of an isolated wing-tip mounted propeller for numerical cross-code validation. The database allows for the assessment of important parameters to predict complex propeller-wing interactional effects and to understand the impact of the propeller on the wing's aerodynamic efficiency.

Within this work, we seek to utilize the extensive and open experimental WIPP database to simulate and validate the flow field of the full WIPP configuration. The open-source multi-physics SU2 solver[8] will be used for the validation exercise. To accurately capture the rich propeller-wing interactional flow physics the blades will be fully resolved and to allow the propeller to move in relative motion to the wing a sliding mesh technique will be used. In so doing, we aim to elucidate the key noise generation mechanisms and visualize the noise footprint both on the propeller and wing surfaces. An important feature within SU2 is the discrete adjoint framework developed on the basis of algorithmic differentiation (AD) which allows for sensitivity analysis and optimal design for both steady and unsteady problems.[9] As a first step towards sensitivity analysis of the full propeller-wing assembly, the unsteady adjoint solver will be used to evaluate the surface sensitivity of the isolated WIPP propeller blades with respect to the time-averaged thrust design objective.

The remainder of this extended abstract is organized as follows. In Section II, the WIPP model, as well as the test conditions are described. In Section III, the multi-physics SU2 solver and the sensitivity analysis framework based on discrete adjoint are presented. Section IV presents the SU2 simulation results and their comparison against experimental data while the conclusion and outlook for furture work are discussed in Section V.

II. WIPP Model Description

The computational test case replicates the WIPP experiment of a wing-tip mounted propeller, as shown on Figure 1. The test took place in the Lockheed Martin Low-Speed Wind Tunnel (LSWT) in Marietta, Georgia, USA as part of the NASA/Armstrong X-57 research program. The WIPP model was designed by Mark Skeehan at Lockheed Martin Aeronautical Systems and was fabricated by Empirical Systems Aerospace (ESAero). The WIPP model is a 40.5%-

scale semi-span model of the X-57, specifically designed to allow it to be mounted onto the LSWT external balance. The model is positioned vertically and incorporates a non-metric boundary layer splitter plate which is mounted to the LSWT external balance. The span of the wing relative to the wind tunnel floor is 67.065 inches. The wing has a taper ratio of 0.7 and an aspect ratio of 6.7. The chord of the wing at its root is 11.6 inches and the chord of the wing at its tip is 8.6 inches. The mean aerodynamic chord of the wing can then be considered as 10.15 inches. The wing also contains a slight leading-edge sweep of 1.9°. The model uses a four-bladed propeller system based on an already available 10%-scale C-130 model. The propeller diameter is 16.2 inches. The propeller blades are calibrated for a 38° pitch at the root and have a significant negative twist from the root to the tips of the blades. The propeller is mounted onto a nacelle at the wing tip. The nacelle is 24.15 inches long and has a maximum diameter of 4.75 inches at its center before being tapered and rounded at the leading and trailing edges.

To measure the interactional effect of the propeller on the wing, the model was instrumented with a total of 96 static pressure taps which were located at six different wing spanwise locations. These spanwise locations were 34, 44, 54, 57, 60.75 and 63 inches from the wind tunnel floor. Each of these spanwise sections then contained 10 static pressure taps on the upper surface and 6 static pressure taps on the lower surface. Wake data also captured the flow-field behind the propeller, nacelle and wing during the experiment using a wake survey system. This system used a wake rake which contained a total of twelve 7-hole pressure probes mounted on a strut 3.0 inches apart.

The tests were then conducted at a variety of Mach numbers, thrust coefficients, and angles-of-attack. The flight speeds investigated were Mach 0.04, 0.08, and 0.11. To achieve variations in the thrust coefficient, the rotational speed of the model propeller was altered. The thrust coefficients investigated ranged from $C_T = 0 \rightarrow 0.40$. There were then three different angle-of-attack schedules planned termed A1, A2, and A3 which ranged from -10 $\rightarrow$ +20 degrees.

Various experimental configurations were also tested for the calibration of the instrumentation, for the assessment of the effectiveness of the ailerons during flow separation, and for determining the influence of the propeller on the performance of the wing. The configurations tested hence included an empty wind tunnel with the model removed, an isolated wing, and an integrated wing and propeller. In total 198 test runs were completed.

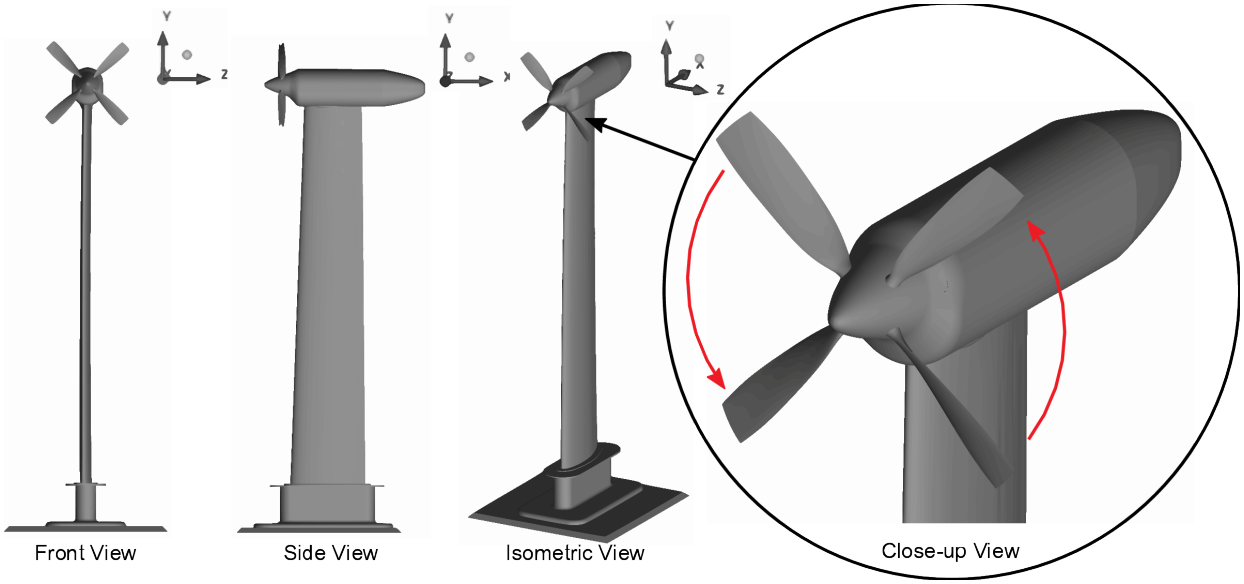

Figure 1: The wing-tip mounted propeller configuration

III. Prediction and Sensitivity Analysis Methodologies

III.A. Turbulent Flow Simulation using SU2

The SU2 open-source software suite was specifically developed for solving problems governed by partial differential equations (PDEs) and PDE-constrained optimization problems. It was developed with the aerodynamic shape optimization problems in mind. Therefore the suite is centered around a Reynolds-averaged Navier-Stokes (RANS) solver capable of simulating compressible, turbulent flows commonly found in problems in aerospace engineering. The governing equations are spatially discretized using the finite volume method, on unstructured meshes. A number of

convective fluxes discretization schemes have been implemented, such as the Jameson-Schimdt-Turkel (JST) scheme and the upwind Roe scheme. The turbulence can be either modeled by the Spalart-Allmaras(S-A) model or the Menter Shear Stress Transport (SST) Model. For unsteady flows, a second-order dual time-stepping method can be used to obtain time-accurate solutions.

For scale-resolving capabilities, the enhance delayed detached eddy simulation (EDDES) based on the S-A model was implemented in SU2 by Molina[10] and has been demonstrated to successfully predict separated flows.[11,12] To mitigate the "grey area" problem characterized by slow transition from RANS to LES mode in the shear-layer, a shear-layer adapted (SLA) sub-grid scale model[13] was implemented. In addition, to limit the numerical dissipation in LES part of the EDDES model, the inviscid flux is computed using the so-called simple low dissipation advection upstream (SLAU2).[14]

For the sake of conciseness, details regarding the formulations and implementations of the SU2 solver suite will not be presented in this paper. Further details such as mesh deformation, dynamic mesh movement, multigrid implementations, validation and verification cases, as well as the continuous adjoint framework developed in tandem with SU2, can be found in the work published by Palacios et al.[15] of the SU2 team. In the next section we direct the attention of the readers to the AD-based discrete adjoint optimization framework used for the current work.

III.B. AD-based Discrete Adjoint Framework

The implementation of the discrete adjoint formulation in this work is eased by the use of algorithmic differentiation (AD) [a], eliminating the error-prone hand-differentiation of the discretized equations. AD was developed based on the observation that any simulation code, regardless of its complexity is merely a sequence of elementary operations whose differentiation rules are well known. Therefore, by successive applications of the chain-rule through the computer program, it is possible to compute both the simulation output and its derivative with respect to prescribed design variables simultaneously. A remarkable feature of AD, owing to its construction, is that it does not incur any truncation errors compared to the traditional finite difference method. In particular, the derivatives are accurate to machine accuracy. This is a very attractive characteristic of AD, since accurate evaluation of the gradient requires exact differentiation of the fixed point iterator G^n as evidenced by Equations 14 and 15 in the following discussion.

Now we present our AD-based unsteady discrete adjoint framework using a simple system of PDEs as an example. For the sake of brevity, influences of the mesh are omitted. Consider a system of semi-discretized PDEs as follows:

$$\frac{dU}{dt} + R(U) = 0 \tag{1}$$

where U is the spatially discretized state vector and $R(U)$ is the discrete spatial residual vector. For the sake of illustration, we assume the second-order backward difference is used for time discretization, which leads to the following system of equations:

$$R^*(U^n) = \frac{3}{2\Delta t}U^n + R(U^n) - \frac{2}{\Delta t}U^{n-1} + \frac{1}{2\Delta t}U^{n-2} = 0, \qquad n = 1,\ldots,N \tag{2}$$

The application of dual-time stepping method then solves the following problem through a fictitious time τ to converge to a steady state solution in (2):

$$\frac{dU^n}{d\tau} + R^*(U^n) = 0 \tag{3}$$

Further assume the implicit Euler method is used to time march the above equation to steady state.

$$U^n_{p+1} - U^n_p + \Delta\tau R^*(U^n_{p+1}) = 0, \qquad p = 1,\ldots,M \tag{4}$$

The resultant nonlinear system can be linearized around U^n_p to solve for the state U^n_{p+1}

$$U^n_{p+1} - U^n_p + \Delta\tau \left[R^*(U^n_p) + \frac{\partial R^*}{\partial U}\bigg|^n_p (U^n_{p+1} - U^n_p) \right] = 0, \qquad p = 1,\ldots,M \tag{5}$$

This can be written in the form of a fixed-point iteration:

$$U^n_{p+1} = G^n(U^n_p, U^{n-1}, U^{n-2}), \qquad p = 1,\ldots,M, \quad n = 1,\ldots,N \tag{6}$$

[a] performed using AD tool ADEPT[16]

where G^n represents an iteration of the pseudo time stepping. U^{n-1} and U^{n-2} are the converged state vectors at time iterations $n-1$ and $n-2$ respectively. The fixed point iteration converges to the numerical solution U^n:

$$U^n = G^n(U^n, U^{n-1}, U^{n-2}), \qquad n = 1, \ldots, N \tag{7}$$

The discrete optimization problem can then be posed as:

$$\min_{\alpha} \qquad J = f(U^{N_*}, \ldots, U^N, \alpha) \tag{8}$$

$$\text{subject to} \qquad U^n = G^n(U^n, U^{n-1}, U^{n-2}, \alpha), \qquad n = 1, \ldots, N \tag{9}$$

where α is the vector of design variables and the objective function J is evaluated between $N_* \leq n \leq N$. One can express the Lagrangian associated with the above constrained optimization problem as follows:

$$L = f(U^{N_*}, \ldots, U^N, \alpha) - \sum_{n=1}^{N} [(\bar{U}^n)^T (U^n - G^n(U^n, U^{n-1}, U^{n-2}, \alpha))] \tag{10}$$

where $\bar{U}^n$ is the adjoint state vector at time level n. The first order optimality conditions are given by:

$$\frac{\partial L}{\partial \bar{U}^n} = 0, \quad n = 1, \ldots, N \qquad \text{(State equations)} \tag{11}$$

$$\frac{\partial L}{\partial U^n} = 0, \quad n = 1, \ldots, N \qquad \text{(Adjoint equations)} \tag{12}$$

$$\frac{\partial L}{\partial \alpha} = 0, \qquad \text{(Control equation)} \tag{13}$$

From (12), the unsteady discrete adjoint equations can be derived in the fixed point form as:

$$\bar{U}^n_{i+1} = \left(\frac{\partial G^n}{\partial U^n}\right)^T \bar{U}^n_i + \left(\frac{\partial G^{n+1}}{\partial U^n}\right)^T \bar{U}^{n+1} + \left(\frac{\partial G^{n+2}}{\partial U^n}\right)^T \bar{U}^{n+2} + \left(\frac{\partial f}{\partial U^n}\right)^T, \; n = N, \ldots, 1 \tag{14}$$

where $\bar{U}^{n+1}$ and $\bar{U}^{n+2}$ are converged adjoint state vectors at time levels $n+1$ and $n+2$. The unsteady adjoint equations above are solved backward in time. At each time level n we iterate through inner iteration i until we have converged to $\bar{U}^n$. The highlighted terms here are evaluated in reverse mode AD at each iteration. To do so, reverse accumulation[17] is performed at the beginning of each time level n to store the computational graph by evaluating G using converged state solution U_n. Then each inner iteration i proceeds by re-evaluating the tape using the updated adjoint vector $\bar{U}^n_i$, giving the highlighted terms. This continues within each time level n until the adjoint vector has converged to $\bar{U}^n$. Note that $\frac{\partial f}{\partial U^n} = 0$ for $n < N_*$. The sensitivity gradient can then be computed from the adjoint solutions:

$$\frac{dL}{d\alpha} = \frac{\partial f}{\partial \alpha} + \sum_{n=1}^{N} \left((\bar{U}^n)^T \frac{\partial G^n}{\partial \alpha}\right) \tag{15}$$

IV. Results

IV.A. Test Conditions

The preliminary simulation results of the WIPP wind tunnel test are based on the fully integrated wing and propeller configuration. Run numbers 33 and 80 of the experimental database were used for the validation of the flow field. The test conditions from run number 33 and 80 are shown in Table 1. The experimental results from run number 33 contain the surface pressure data along the spanwise direction of the wing and the experimental results from run number 80 contain the wake survey data. The α schedule used within this run was A3 where the angle-of-attack ranged from -10 $\rightarrow$ +20 degrees, however, only $\alpha = 0.0$ was considered during the early stages of this work. The flight speed of this run was the highest tested in the LSWT at Mach = 0.11. The wind tunnel freestream pressure, at this flight speed was recorded and measured as Q = 18.31 lbf/ft^2. The mean aerodynamic chord of the wing was used as the reference length for computing the Reynolds number of flow field and was computed to be Re = 0.660×10^6. The propellers were approximately rotating at 8000RPM to achieve a thrust coefficient of $C_T = 0.4$.

Table 1: Configuration and Parameters.

Configuration	α Schedule	Mach [-]	Q [lbf/ft^2]	Re [-]	C_T [-]	Run No
Integrated Wing and Propeller	A3	0.11	18.31	0.660×10^6	0.4	33, 80

IV.B. Mesh Generation

The simulation of propeller-wing interactions are rich in flow physics and so require a high fidelity of computational modeling. Thus, to allow the propeller to move in relative motion to the wing the numerical discretization of the mesh is required. Within this work, the sliding mesh technique is used to allow the propeller to rotate while the wing remains stationary. The sliding mesh implementation used within SU2 is based on the super-mesh approach described by Rinaldi et al.[18] and allows for flux-conserving treatment of non-conformal interfaces. The numerical discretization of the mesh used within this work is shown in Fig. 2 and shows the cylindrical cut-out where the propeller is positioned. The mesh is hereafter considered as a multi-zone problem where the external stationary zone and the internal rotating internal zone are considered as separate entities and a nearest-neighbour interpolation technique is used for data exchange between the zone interfaces.

To simplify the generation of the mesh, the clamp at the base of the wing was not considered since there was no pressure tap measurements and wake data collected this close to the root of the wing. An artificial wall was then introduced into the simulation where the root of the wing meets the external balance at $y = 7.115$ in. using euler boundary conditions to avoid the need of modelling the boundary layer of the artificial wind tunnel floor. The leading edge of the nacelle was also reconstructed in order to insert the sliding mesh surface interfaces. With the reduction in the length of the nacelle being only slight and with there being no wake data recorded in this region due to it being too close to the propeller this assumption was justified. Artificial wind tunnel inflow and outflow walls were placed at 25 propeller radii upstream and downstream of the model propeller and wing at $x = \pm 25$R. Wind tunnel walls were also placed above the model at $y = 15$R and either side of the model at $z = \pm 10$R.

The stationary zone containing the wing and nacelle consists of mixed quadrilateral and triangular surface elements elements. The rotating propeller surface mesh uses triangular elements. The boundary layer of the wing, nacelle and propeller is sufficiently resolved to ensure $y^+ < 1$. Tetrahedral volume elements are used outside of the boundary layer. The rotating internal boundary interface and stationary external boundary interface both use entirely triangular surface elements.

A prerequisite for accurate wake modeling of the WIPP configuration is a high-quality and high resolution mesh in the region behind the propeller to preserve the main blade-tip vortices and smaller scale vortex structures. Suitable refinement is important to reduce numerical dissipation of the wake so that blade-tip vortex/wing interaction effects are correctly modeled. The importance of the mesh refinement region in the near-field propeller wake around the nacelle is thus studies in this work. Three levels of refinement are evaluate with different node distributions. The details of the individual grids is outlined in Table 2.

Table 2: Details of the three levels of grid refinement.

Name	No. Volume Elements			Wake Element Size*	Density Region
	Propeller	Wing	Total	(l/c_{tip})	
Grid-01 (G1)	5.14M	5.8M	10.9M	0.4195	No
Grid-02 (G2)	12.3M	23.0M	35.3M	0.167	No
Grid-03 (G3)	12.3M	52.6M	64.9M	0.0682	Yes

* cell edge length l non-dimensionalized by blade tip chord c_{tip}, measured at a distance $0.5R_{\text{prop}}$ behind the tip of the propeller.

Grid G1 has the lowest refinement in this study and is shown in Fig. 2a. In G1 there are 5.14M elements in the internal propeller zone and 5.8M elements in the external wing zone. In total, the combined number of elements across both zones is 10.9M. It has a maximum surface element size of 0.004m which expand at a ratio of 1.2 away from the surface. The distribution of elements in the near-field wake region is shown more closely in Fig. 2d. This leads to a computational efficient solution at the expense of the wake accuracy. Grid G2 has a higher refinement than grid G1 and is shown in Fig. 2b. There are 12.3M elements in the internal propeller zone and 23.0M elements in the external wing zone. In total, the combined number of elements across both zones is 35.3M. It has a maximum surface element

size of 0.004m which expand at a ratio of 1.05 away from the surface. The distribution of elements in the near-field wake region is shown more closely in Fig. 2e. This improves wake refinement globally over the entire span of the wing as well as the propeller wake. In the positive y-direction away from the nacelle and towards the blade tip the wake however naturally begins to coarsen. Grid G3 has the highest refinement of all the grids and is shown in Fig. 2c. In G3 there are 12.3M elements in the internal propeller zone and 52.6M elements in the external wing zone. In total, the combined number of elements across both zones is 64.9M. It has a maximum surface element size of 0.002m which expand at a ratio of 1.1 away from the surface. Increasing the expansion ratio allowed for points with minimal influence, such as close to the wing root where there is no measured wake data, to be redistributed elsewhere. A local density region was then placed around the nacelle and propeller wake with a maximum element size of 0.003m in this region. The distribution of elements in the near-field wake region is shown more closely in Fig. 2f. This further improved the wake refinement however only locally and in the critical area to minimize the computational cost where possible.

IV.C. Aerodynamic Prediction

The simulation are performed on all three grids using unsteady RANS with Spalart-Allmaras turbulence model (URANS-SA). In addition, EDDES-SA simulations are also performed on grids G2 and G3 in attempt to better resolve the turbulent wake behind the propeller. A total of 15 propeller revolutions are simulated. The flow statistics are computed over the last 10 revolutions. The physical time step is $2.1 \times 10^{-5} s$ which is equivalent to 1° of revolution per time step at approximately 8000RPM.

The static pressure tap measurements recorded during run number 33 are used for validation of the chordwise pressure coefficient distribution along spanwise sections of the wing. The conditions simulating $M_\infty = 0.11$ corresponds to the highest dynamic pressure obtained throughout the experimental test campaign. The numerical results of the mean pressure coefficient at six different spanwise locations along the wing are shown in Fig. 4. Pressure tap locations $y = 34.386$ in., $y = 44.386$ in., and $y = 54.386$ in. are outwith the propeller slipstream. Pressure tap location $y = 57.386$ in. is aligned approximately 1.5 in. outward of the propeller tip. Pressure tap locations at $y = 60.955$ in. and $y = 63.469$ in. are directly in the propeller slipstream. The results shown begin close to the root of the wing and progressively get closer towards the tip of the wing. Time-averaged URANS-SA predictions on grid G1 are used for comparison with experimental data. The predicted pressure coefficient distributions at the spanwise locations outwith the propeller wake are in close agreement with the measured data and are shown in Fig. 4a-4c. The predicted pressure coefficient distribution at the spanwise location which corresponds to being marginally outward of the blade tip is shown in Fig. 4d. It illustrates that the pressure tap is beyond the wake of the propeller which the prediction captures. The predicted pressure coefficient distributions at the spanwise locations inside the propeller slipstream are shown in Fig. 4e & 4f. The interaction effects of the propeller slipstream at these spanwise locations are shown to have a significant influence on the pressure coefficient distributions, leading to a clear suction peak near the wing leading edge on the blade retreating side. This dynamic effect is more challenging to simulate and accurately model however the blade-tip vortex disturbances on the surface of the wing appear to well represented. Overall, the computed pressure coefficient is in good agreement with the measured data from run number 33. This close agreement is particularly true for the results outwith the influence of the propeller. As the influence of the propeller becomes apparent slight discrepancies arise, however despite this, the suction peak is well captured.

The wake rake measurements recorded during run number 80 are used for validation of the downstream propeller velocity profile and performance characteristics. The velocity profile is decomposed into the separate velocity components to obtain the normal velocity, swirl velocity and radial velocity. The propeller performance is separated into the propeller thrust distribution and torque distribution. The thrust and torque distributions are computed respectively as,

$$\text{Thrust} = \int_0^{2\pi} \int_0^{R_{\text{prop}}} \rho U \left(U - U_\infty\right) r dr d\Theta, \qquad \frac{\text{Thrust}}{Q_\infty R_{\text{prop}}^2} = 2\pi \int_0^1 \frac{\rho U \left(U - U_\infty\right)}{Q_\infty} \frac{r}{R_{\text{prop}}} d\frac{r}{R_{\text{prop}}}. \tag{16}$$

$$\text{Torque} = \int_0^{2\pi} \int_0^{R_{\text{prop}}} \rho U W_{\text{swirl}} r dr d\Theta, \qquad \frac{\text{Torque}}{Q_\infty R_{\text{prop}}^3} = 2\pi \int_0^1 \frac{\rho U W_{\text{swirl}}}{Q_\infty} \left(\frac{r}{R_{\text{prop}}}\right)^2 d\frac{r}{R_{\text{prop}}} \tag{17}$$

where the area to the left of the thrust and torque distributions integrates to the total thrust and total torque. The predictions use the thrust and torque distributions to compare against the measured data. The strong relationship between the normal velocity and thrust, and, the swirl velocity and torque is the rationale behind also comparing the normal and swirl components of the velocity profiles with the measured data.

The experimental wake data was measured at five locations downstream of the propeller in the positive x-direction. The measurements were record at 2.65 in., 6.15 in., 14.15 in., 22.15 in., and 42.15 in. downstream from the propeller plane. These measurement locations correspond to positions $x = 1.5$ in., $x = 5.0$ in., $x = 13.0$ in., $x = 21.0$ in., and $x = 41.0$ in. in the mesh coordinate system. As a safety precaution, measurements were not recorded any closer to the propeller. This work focuses on the four critical locations closest to the propeller due to these being in the near-field wake of the propeller. The fifth position is significantly further from the nacelle's trailing edge and given the computational and time constraints it is currently not feasible to include in the current simulations. Future work will however seek to consider the fifth wake location.

The predicted normal and swirl velocity at the four wake stations are respectively shown in Fig. 5 and Fig. 6. The velocity profiles closest to the propeller at position $x = 1.5$ in. are predicted well in Fig. 5a and Fig. 6a. Notably, the swirl velocity, given that it is particularly challenging to capture. The difference between the coarse and fine grid results are minimal. The same can be said for the URANS and EDDES comparison this close to the propeller. Slight differences only arise just beyond $R/R_{\text{prop}} = 1$. Progressing downstream, to the wake stations at positions $x = 5.0$ in., $x = 13.0$ in., and $x = 21.0$ in. as shown in Figs. 5b-5d and Figs. 6b-6d, a trend emerges and the simulations performed on the finest grid (G3) prevail. Discrepancies between simulations on the three grid levels increase further downstream. The finest grid (G3) results show limited influence of grid dissipation evidenced by the peaks of the velocity profiles maintaining their strength to the furthest position from the propeller at $x = 21.0$ in. as depicted by Fig. 5d and Fig. 6d. At this location there are significantly different results between the grids at $R/R_{\text{prop}} = 1$. A general trend of the predictions at each location is that the velocity profiles appear to be shifted radially inwards. The predictions suggest that the velocity profiles produced by the propeller do not extend beyond $R/R_{\text{prop}} = 1$ as suggest by the wake survey.

The predicted thrust and torque distribution at the four wake stations are respectively shown in Fig. 7 and Fig. 8. The thrust and torque distributions shown in Eq. 16 and Eq. 17 are used for comparison with wake survey. From these relationships, it is apparent that the influence of the normal velocity on the thrust distribution, and, the swirl velocity on the torque distribution, is significant and thus, similar trends are expect to the results illustrated in Fig. 5 and Fig. 6. The thrust and torque distributions closest to the propeller at position $x = 1.5$ in. are predicted closely to the measured data in Fig. 7a and Fig. 8a. Similarly to the velocity profiles, it is observed that the differences between the thrust and torque predictions increase at the downstream locations as shown in Figs. 7b-7d and Figs. 8b-8d. The finest grid (G3) results show limited influence of grid dissipation evidenced by the thrust and torque distribution peaks maintaining their strength to the furthest position from the propeller at $x = 21.0$ in. as depicted by Fig. 7d and Fig. 8d. Overall, the performance characteristics tend to be predicted radially inwards and the distribution peaks are slightly under predicted when compared against the measurements. The simulations suggest that the propeller produces its peak performance between $R/R_{\text{prop}} = 0.8 - 0.95$ whereas the wake survey suggests the propeller produces its peak performance at the propeller tip $R/R_{\text{prop}} = 1$ and even slightly beyond.

A summary of the normal and swirl velocity profiles and thrust and torque distributions is deduced. The general observation on all four quantities of interest predicted in the wake are:

- Grid G1 is too coarse and therefore too dissipative to accurately capture the wake profiles at the downstream locations $x = 5.0$ in., $x = 13.0$ in., and $x = 21.0$ in..
- While better agreement with experiment is obtained using grids G2 and G3, they still significantly under-predict the peak values of the normal velocity and thrust distribution. The observation of the swirl velocity and torque distribution is markedly improved however they remain below the measured peaks.
- While the general shapes of all wake profiles are well captured for grids G2 and G3, the predicted profiles all show a downward offset when compared with the wake measurement data. The same observation has also been made in numerical results of many participants in the last WIPP workshop. This may indicate a systematic measurement error.
- No discernible improvement in the wake profile prediction is achieved when switching from URANS to EDDES. This indicates that even grid G3 may still be too coarse for the wake to develop in a physically plausible manner when EDDES is supposedly operating in the LES mode in that region. As shown on Table 2, the ratio between the edge length of a cell in the wake and the tip chord of the propeller is 0.0682 for G3 – much larger than the typical value of 0.01 or less often used for scale-resolving simulations.

To help visualize the highly three-dimensional nature of the problem the Q-criterion colored by dimensionless streamwise velocity is shown in Fig. 9 for the URANS-SA simulations performed on all 3 grids and in Fig. 10 for

the EDDES-SA simulations performed on G2 and G3. The vortical structures are preserved and persist further downstream as the grid is refined. In addition, the EDDES simulations further resolve smaller turbulence structures in the wake region compared to their URANS counterparts. The EDDES-SA simulation on G3 clearly reveals two major interactional noise sources: the turbulent wake and tip vortex generated by the propeller blades, both impinging upon the wing and nacelle surfaces as they convect downstream. In addition, the secondary vortex emanating from the trailing edge of the blade tip is also captured. It is this interactional behaviour close to the propeller which influences the pressure coefficient on the wing displayed in Fig. 4e & 4f.

In light of the promising aerodynamic results, progression towards the prediction of the aeroacoustics was the subsequent area of interest. As a first step in assessing the noise sources in this integrated wing-propeller configuration, the instantaneous pressure fluctuations over the full configuration captured by URANS and EDDES simulations on G3 are shown in Fig. 11. The locations at which the blade-tip vortices impact on the wing and nacelle correlate into strong noise sources, as evidenced by the alternating pressure fluctuation patterns near the wing-tip below the nacelle. In addition, the turbulent wake shed by the propeller blades leaves spiralling patterns around the nacelle surface. EDDES appears to capture the finer features of the surface pressure fluctuation patterns much more clearly, especially around the nacelle.

The surface 'noise footprint' is visualized by the root-mean-square of the pressure fluctuation and shown in Fig. 12. The dominant noise source is located at the leading edge of the wing immediately below the nacelle where the tip vortex in the propeller slipstream makes first contact with the wing surface. This is consistent with the findings of Avallone et al. in their computational aeroacoustic study of a similar configuration.[7] From a noise reduction perspective, this indicate that in addition to optimizing the shape of the blades, it may also be highly effective to consider also optimally morphing the leading edge of the wing in the slipstream.

IV.D. Adjoint Sensitivities

The discrete adjoint-based framework described in Section III.B is used to evaluate the surface design sensitivities with respect to the mean thrust coefficient $\bar{C}_T$ of the isolated WIPP propeller. To that end, the primal simulation is first performed over 8 revolutions to exclude the transient effects. The adjoint sensitivities are then evaluated for the time-averaged C_T over the next 2 full revolutions. The design sensitivities in the surface normal direction on the windward and leeward sides of the propeller are shown on Figure 13. Highly sensitive regions where shape deformations will effect the maximum changes in the design objective are clearly visualized to be along the tip and the leading and trailing edges of the blades.

It should be noted that the adjoint-based framework allows the evaluation of such design sensitivities efficiently, at a computational cost independent of the number of design variables. The four blade surfaces contain almost 8000 mesh points – a non-adjoint-based approach would lead to a prohibitively high cost in the gradient evaluation, especially if the full wing-propeller assembly is considered.

Furthermore, while the objective function is defined to be the mean C_T for the current result, the AD-based discrete adjoint framework provides the flexibility to redefine the objective function to any user-defined expression that represents aerodynamic efficiency or far-field noise level of the isolated propeller or the full wing-propeller configuration. For a shape optimization study to be conducted in the near future, to ensure smooth shape deformations, the surface sensitivities will be projected to a set of free-form deformation (FFD) control points[19] which are used to parameterize the surface and allow it deform smoothly like an elastic solid.

V. Conclusion

In this work, we simulate the turbulent flow field around a wing-tip mounted propeller configuration using the model and test conditions released by the Workshop for Integrated Propeller Prediction (WIPP). In particular, the unsteady RANS equations with Spalart-Allmaras turbulence model (URANS-SA) are solved in a time-accurate manner with the multi-zone sliding mesh technique in which the propeller is allowed to rotate while the wing and the nacelle remain stationary. In addition, enhanced delayed detached eddy simulations based on the Spalart-Allmaras model (EDDES-SA) are performed on the finer grids in an attempt to better resolve the turbulent wake behind the propeller. Current results are based on the test conditions from run number 33 and 80, namely $M_\infty = 0.11$, $C_T = 0.40$ and $AoA = 0^\circ$.

Time-averaged pressure coefficients at six spanwise locations along the wing surface are shown to be in good agreement with the experimental data. The two locations in the propeller slipstream in particular closely resemble the measurements and capture the blade-wing interaction effects. Time-averaged wake profiles of normal velocity, swirl velocity, thrust distribution and torque distribution at four stations downstream of the propeller are compared

with experimental data from the wake survey. In general, while the overall shapes of all profiles are captured correctly on finer grids, the peak values are under-predicted on all wake profiles except for the swirl velocity. Moreover, there appears to be a shift radially inward indicating that the wake quantities, and the thrust in particular, do not extend beyond the propeller tip, as suggested by the experiment. Supplementary to the wake quantity predictions, the Q-criterion iso-surface helps visualize the vortical structures produced by the propeller blades and assess how they interact with wing and nacelle surfaces as they are convected downstream. This highlights the importance of the high level of mesh refinement required for such a complex configuration like a wing-tip mounted propeller. Furthermore, going beyond the original WIPP requirements, aeroacoustic aspects of this configuration are also studied in the current work. Visualization of the surface pressure fluctuations reveals the noise footprints on this integrated propeller-wing system. In particular, the impingement of propeller blade tip vortices on the leading edge of the wing immediately below the nacelle is identified to be the main noise source.

Making inroads into sensitivity analysis of the full propeller-wing assembly, an unsteady discrete adjoint approach based on algorithmic differentiation is applied to evaluate the surface sensitivity of an isolated WIPP propeller with respect to the mean thrust coefficient design objective. The surface sensitivity helps inform the designer the most effective locations on the surface to make changes to minimize/maximize the design objective.

Looking ahead, we intend to improve the mesh resolution in the propeller wake region around the nacelle to approximately 150M elements and reduce the physical time-step to 0.25° of revolution per time step to ensure an even higher resolution of the fine-grained vortical structures for the EDDES simulation. We would also like to assess addition conditions at other Mach numbers, propeller thrust settings and angle of attacks specified by the WIPP workshop and compare our predictions with available experimental data. In addition to build on the current noise footprints, a solid-surface Ffowcs Williams-Hawkings (FWH) method[20] will be used to evaluate the far-field noise level of the configuration using surface pressure data obtained from CFD simulations. Extending from the isolated propeller sensitivity analysis we would like to look at the full integrated propeller-wing configuration to assess the influence of the interaction effects. Finally, we intend to perform two adjoint-based shape optimizations – the first to maximize the aerodynamic efficiency of the integrated wing-propeller system and the second to minimize the far-field noise while maintaining the baseline aerodynamic performance. The shapes of the propeller blades as well as the region of the wing surface in the propeller slipstream will be optimized.

VI. Acknowledgement

The computational resources provided by the RHRK high performance computing center via the 'Elwetritsch' high performance cluster at the TU Kaiserslautern is gratefully acknowledged. The work from Politecnico di Milano would like to acknowledge receiving funding from the European Union's H2020 research and innovation programme under the Marie Skłodowska-Curie grant agreement No 721920. Further information can be found at the Network for Innovative Training on ROtorcraft Safety (NITROS) project website.

References

[1]Mann, S. and Stuart, C., "Advanced propulsion through the 1990s – an airframer's view," *21st Joint Propulsion Conference, AIAA 1985-1192*, 1985.

[2]Moore, M. D., "Misconceptions of electric aircraft and their emerging aviation markets," *52nd Aerospace Sciences Meeting*, 2014, p. 0535.

[3]SNYDER JR, M. H. and ZUMWALT, G. W., "Effects of wingtip-mounted propellers on wing lift and induced drag." *Journal of Aircraft*, Vol. 6, No. 5, 1969, pp. 392–397.

[4]Patterson, Jr, J. and Bartlett, G., "Effect of a wing-tip mounted pusher turboprop on the aerodynamic characteristics of a semi-span wing," *21st Joint Propulsion Conference, AIAA 1985-1286*, 1985.

[5]Miranda, L. and Brennan, J., "Aerodynamic effects of wingtip-mounted propellers and turbines," *4th Applied Aerodynamics Conference, AIAA 1986-1802*, 1986.

[6]Sinnige, T., van Arnhem, N., Stokkermans, T. C., Eitelberg, G., and Veldhuis, L. L., "Wingtip-Mounted Propellers: Aerodynamic Analysis of Interaction Effects and Comparison with Conventional Layout," *Journal of Aircraft*, Vol. 56, No. 1, 2019, pp. 295–312.

[7]Avallone, F., Casalino, D., and Ragni, D., "Impingement of a propeller-slipstream on a leading edge with a flow-permeable insert: A computational aeroacoustic study," *International Journal of Aeroacoustics*, Vol. 17, No. 6-8, 2018, pp. 1–25.

[8]Economon, T. D., Palacios, F., Copeland, S. R., Lukaczyk, T. W., and Alonso, J. J., "SU2: An open-source suite for multiphysics simulation and design," *Aiaa Journal*, Vol. 54, No. 3, 2015, pp. 828–846.

[9]Zhou, B. Y., Albring, T. A., Gauger, N. R., Economon, T. D., Palacios, F., and Alonso, J. J., "A discrete adjoint framework for unsteady aerodynamic and aeroacoustic optimization," *16th AIAA/ISSMO Multidisciplinary Analysis and Optimization Conference, AIAA 2015-3355*, 2015.

[10]Molina, E., *Detached Eddy Simulation in SU2*, Ph.d. thesis, Aeronautical Institute of Technology, 2015.

[11]Molina, E. M., Zhou, B. Y., Alonso, J. J., Righi, M., and da Silva, R. G., "Flow and Noise Predictions Around Tandem Cylinders using DDES approach with SU2," AIAA-2019-0326, 2019.

[12]Molina, E. S., Silva, D. M., Broeren, A. P., Righi, M., and Alonso, J. J., "Application of DDES to Iced Airfoil in Stanford University Unstructured (SU2)," *Progress in Hybrid RANS-LES Modelling*, edited by Y. Hoarau, S.-H. Peng, D. Schwamborn, A. Revell, and C. Mockett, Springer International Publishing, Cham, 2020, pp. 283–293.

[13]Shur, M. L., Spalart, P. R., Strelets, M. K., and Travin, A. K., "An Enhanced Version of DES with Rapid Transition from RANS to LES in Separated Flows," *Flow, Turbulence and Combustion*, Vol. 95, No. 4, 2015, pp. 709–737.

[14]Kitamura, K. and Hashimoto, A., "Reduced Dissipation AUSM-family Fluxes: HR-SLAU2 and HR-AUSM+-up for High Resolution Unsteady Flow Simulations," *Computers & Fluids*, Vol. 126, 2016, pp. 41–57.

[15]Palacios, F., Economon, T. D., Aranake, A. C., Copeland, S. R., Lonkar, A. K., Lukaczyk, T. W., Manosalvas, D. E., Naik, K. R., Padron, A. S., Tracey, B., Variyar, A., and Alonso, J. J., "Stanford University Unstructured (SU2): Open-source analysis and design technology for turbulent flows," *AIAA Journal*, Vol. 54, 2016, pp. 828–846.

[16]Hogan, R., "Fast reverse-mode automatic differentiation using expression templates in C++," *Transactions on Mathematical Software*, Vol. 40, 2014, pp. 1–16.

[17]Griewank, A. and Walther, A., "Evaluating Derivatives: Principles and Techniques of Algorithmic Differentiation," *Other Titles in Applied Mathematics*, SIAM, 978–0–898716–59–7, 2008.

[18]Rinaldi, E., Colonna, P., and Pecnik, R., "Flux-conserving treatment of non-conformal interfaces for finite-volume discretization of conservation laws," *Computers & Fluids*, Vol. 120, 2015, pp. 126–139.

[19]Sederberg, T. W. and Parry, S. R., "Free-form deformation of solid geometric models," *SIGGRAPH Comput. Graph.*, Vol. 20, 1986, pp. 151–160.

[20]Icke, R. O., Baysal, O., Moy, A., Lopes, L., Zhou, B. Y., and Diskin, B., "Toward Adjoint-Based Aeroacoustic Optimization for Propeller and Rotorcraft Applications," *AVIATION 2020 Forum, AIAA-2020-3140*, 2020.

Figures

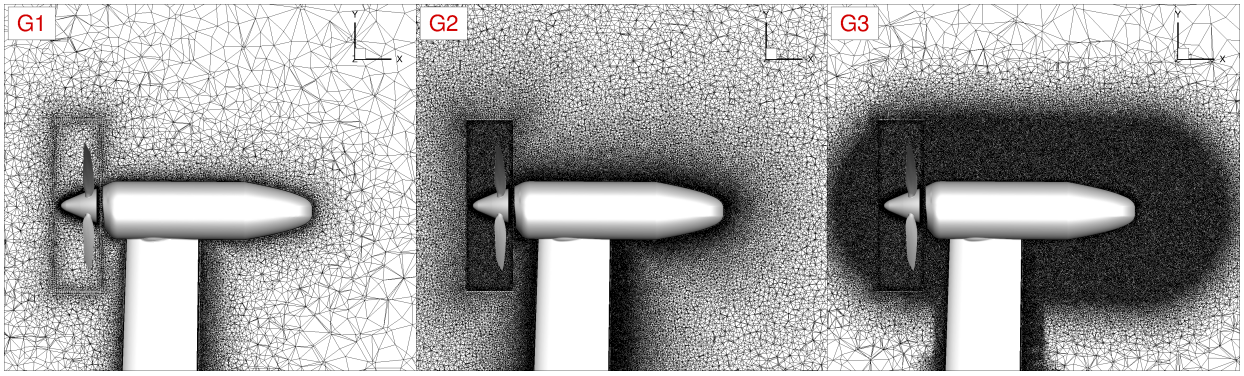

(a) Grid-01 at $z = 0$ in. (b) Grid-02 at $z = 0$ in. (c) Grid-03 at $z = 0$ in.

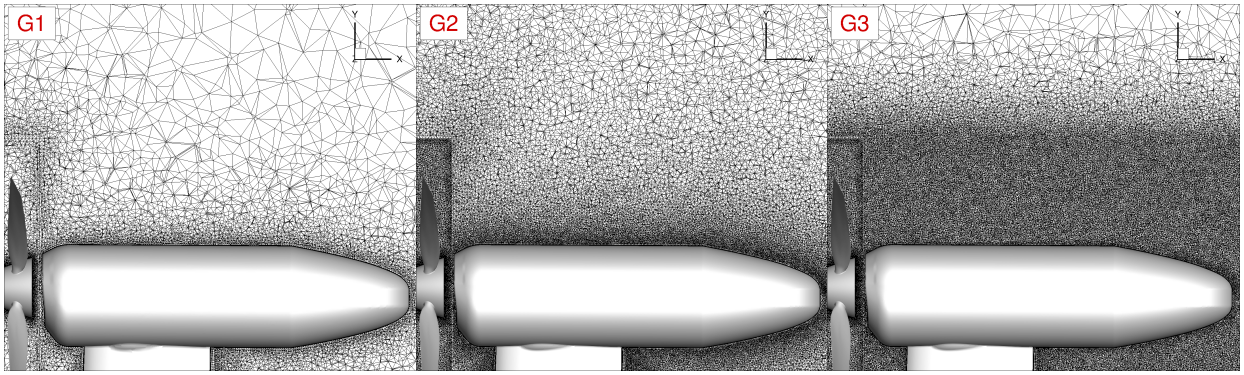

(d) Grid-01 near-field wake refinement (e) Grid-02 near-field wake refinement (f) Grid-03 near-field wake refinement

Figure 2: Spatial resolution of the grids G1, G2, and G3 used for the sensitivity analysis. Displaying the distribution of nodes surrounding the nacelle and near-field wake region.

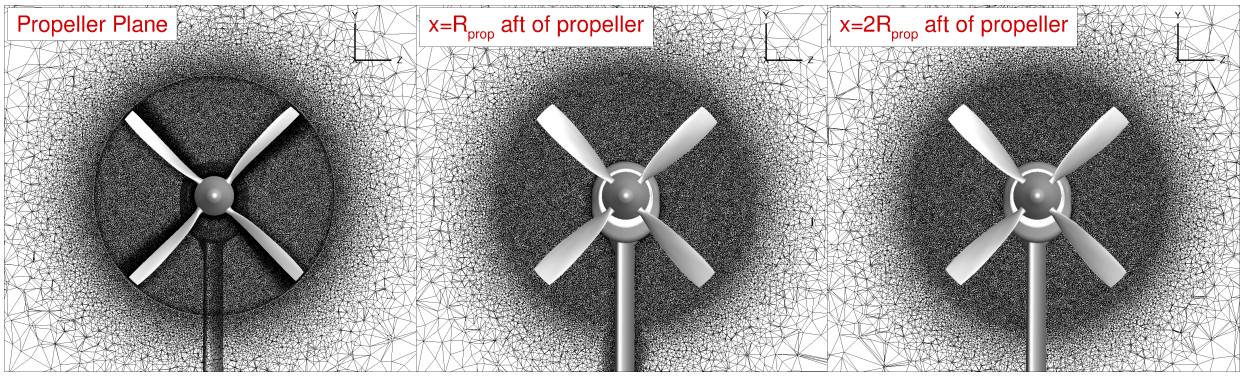

(a) Propeller plane. (b) $x = R_{\text{prop}}$. (c) $x = 2R_{\text{prop}}$.

Figure 3: Spatial resolution of Grid-03 in the $y-z$ plane at the propeller and stations aft of the propeller at $x = R_{\text{prop}}$ and $x = 2R_{\text{prop}}$. Displaying the continuous refinement in the propeller wake region.

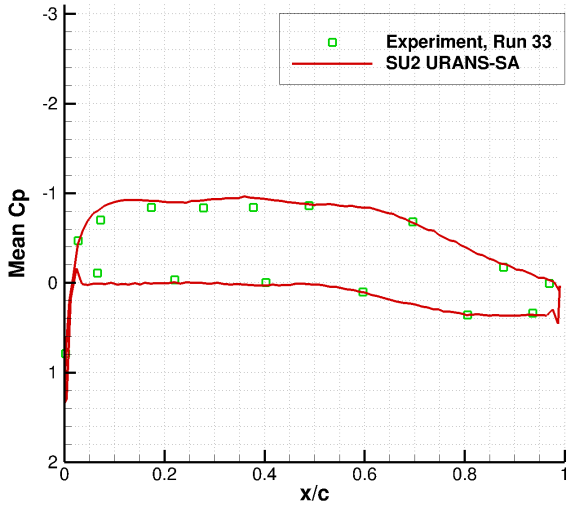

(a) $y = 34.386$ in.

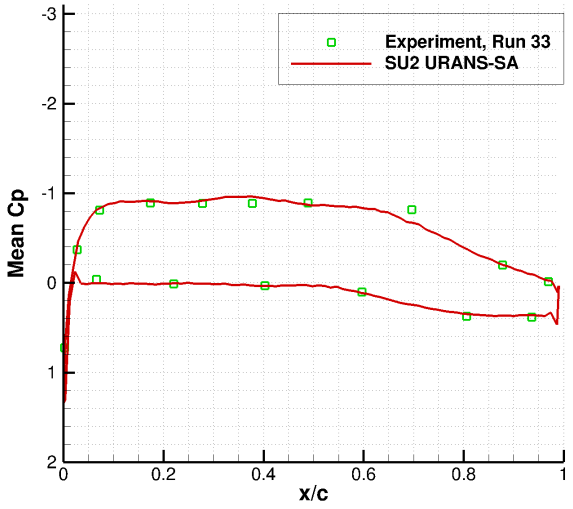

(b) $y = 44.386$ in.

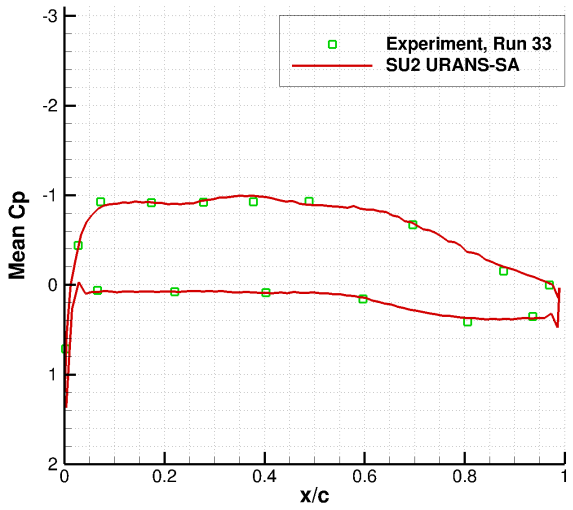

(c) $y = 54.386$ in.

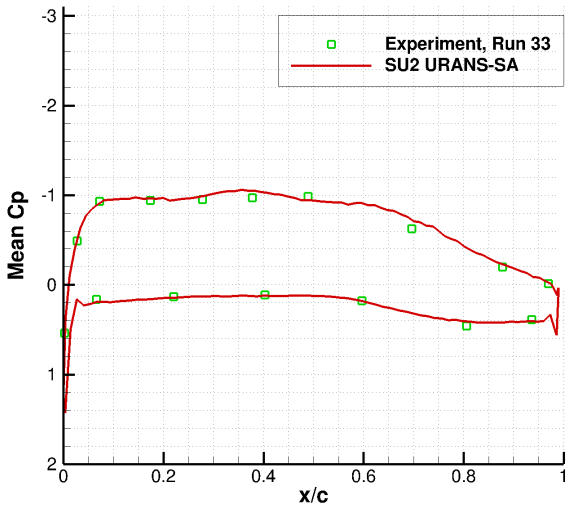

(d) $y = 57.386$ in.

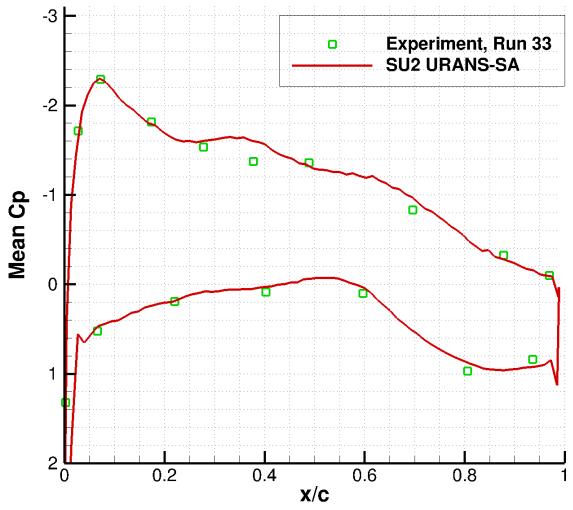

(e) $y = 60.955$ in.

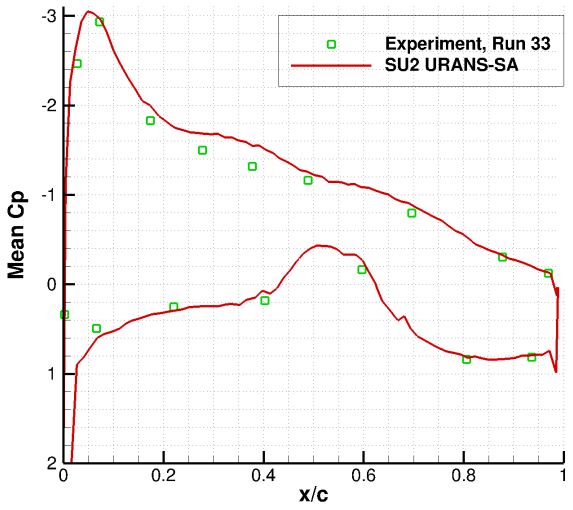

(f) $y = 63.469$ in.

Figure 4: Mean pressure coefficient at six spanwise stations along the wing, $M_\infty = 0.11$, $C_T = 0.40$, $AoA = 0°$

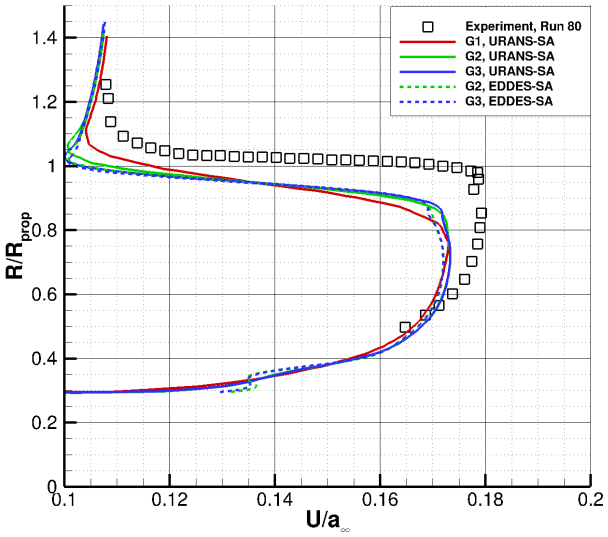

(a) $x = 1.5$ in.

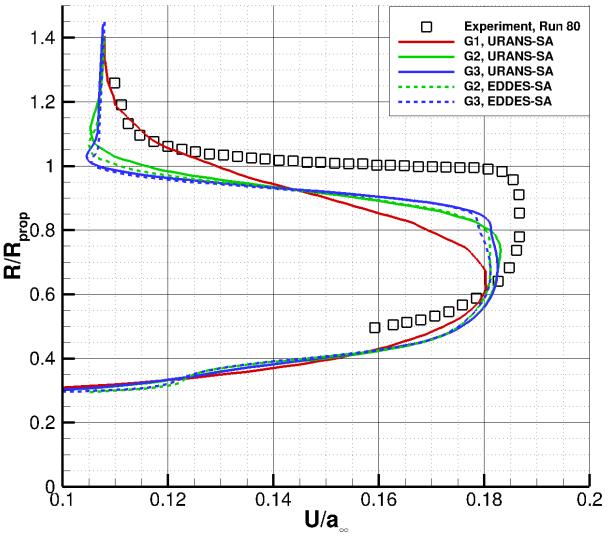

(b) $x = 5.0$ in.

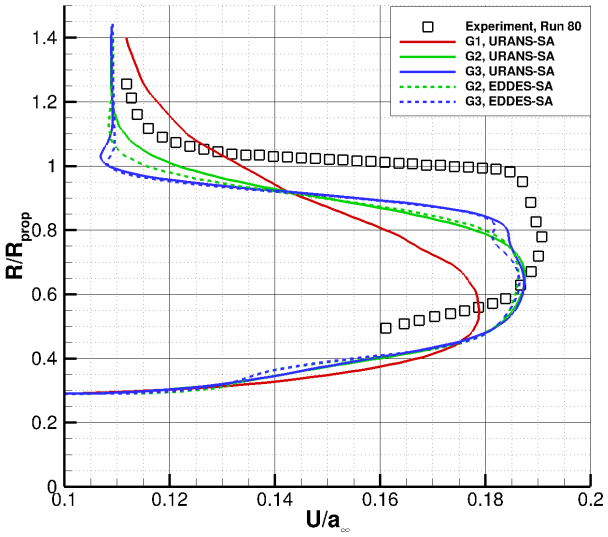

(c) $x = 13.0$ in.

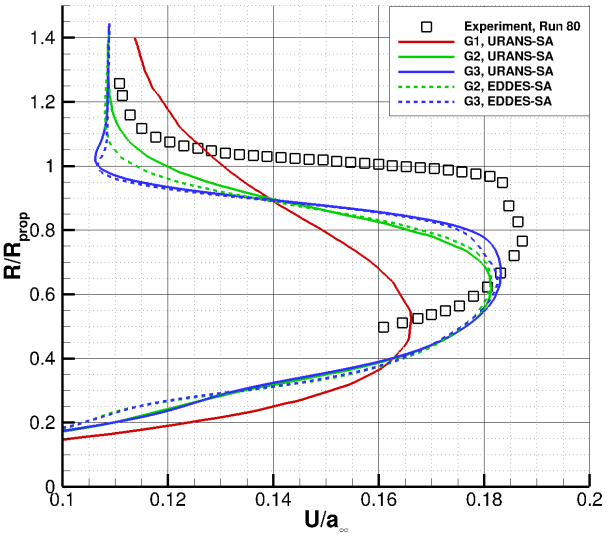

(d) $x = 21.0$ in.

Figure 5: Normal velocity distribution at four stations in the wake of the propeller, $M_\infty = 0.11$, $C_T = 0.40$, $AoA = 0°$

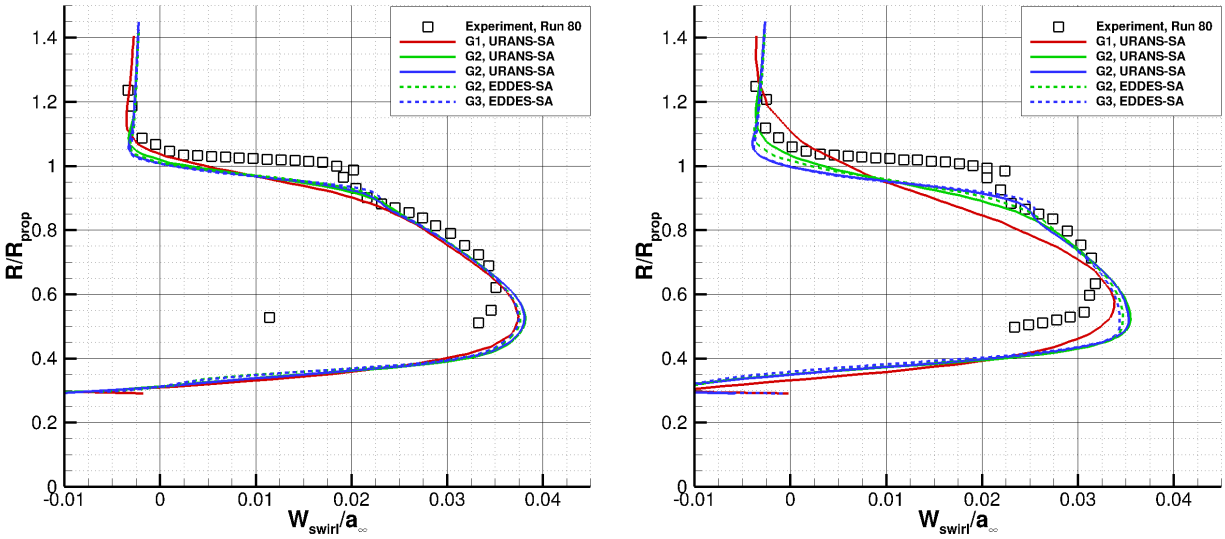

(a) $x = 1.5$ in.

(b) $x = 5.0$ in.

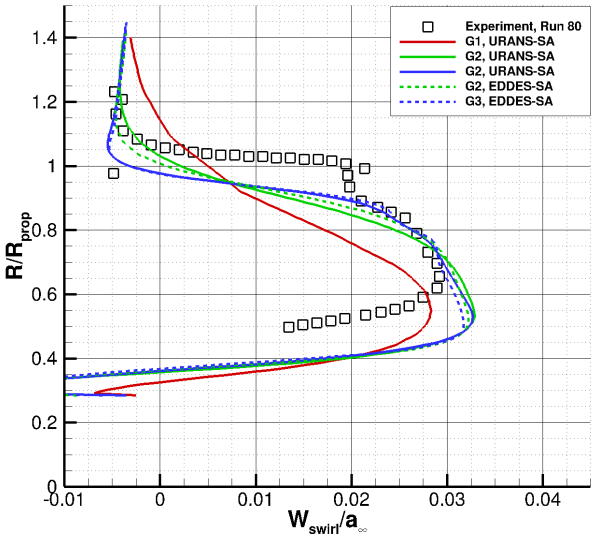

(c) $x = 13.0$ in.

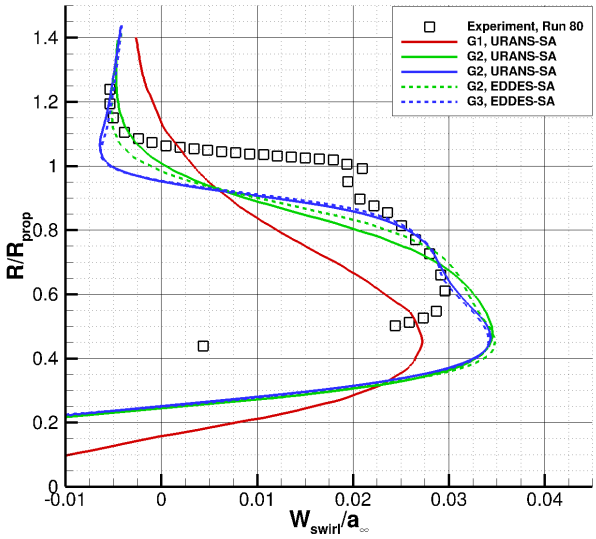

(d) $x = 21.0$ in.

Figure 6: Swirl velocity distribution at four stations in the wake of the propeller, $M_\infty = 0.11$, $C_T = 0.40$, $AoA = 0°$

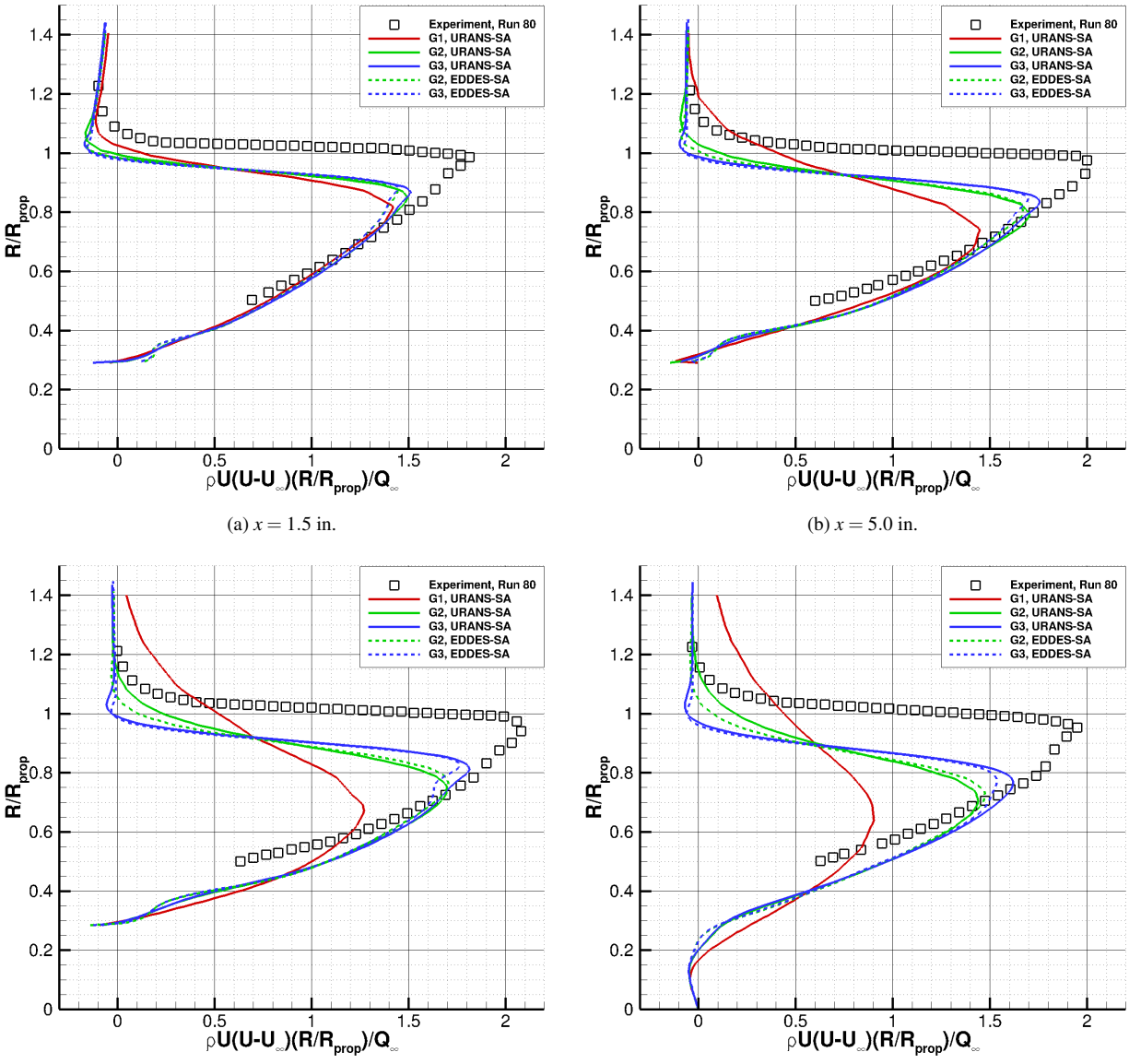

(a) $x = 1.5$ in.

(b) $x = 5.0$ in.

(c) $x = 13.0$ in.

(d) $x = 21.0$ in.

Figure 7: Thrust distribution at four stations in the wake of the propeller, $M_\infty = 0.11$, $C_T = 0.40$, $AoA = 0°$

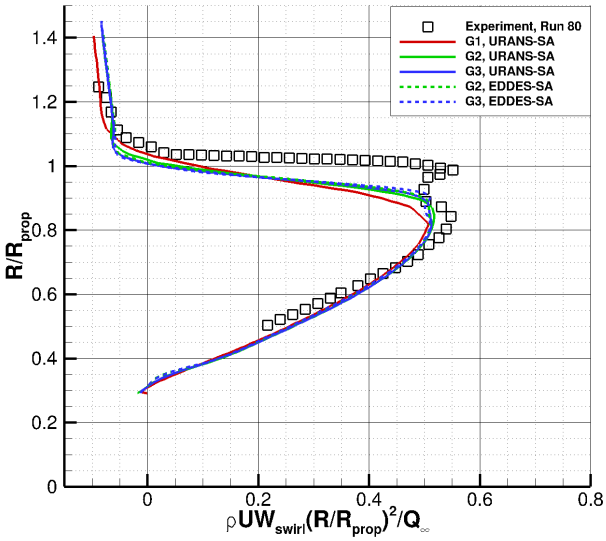

(a) $x = 1.5$ in.

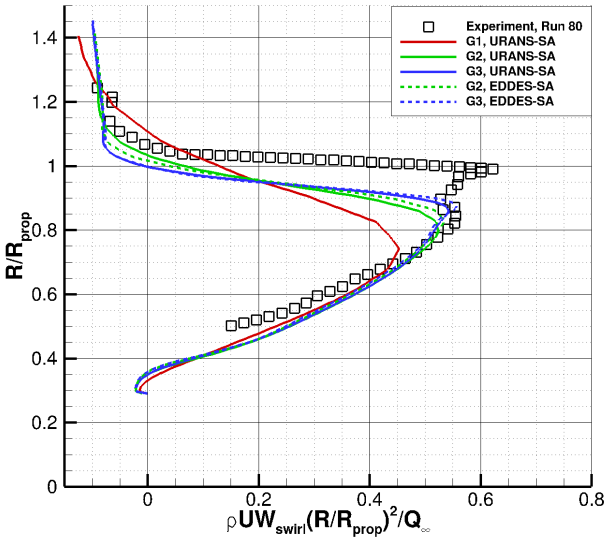

(b) $x = 5.0$ in.

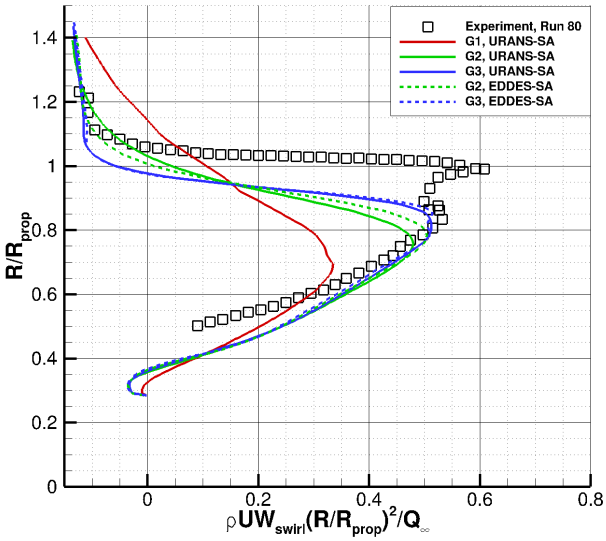

(c) $x = 13.0$ in.

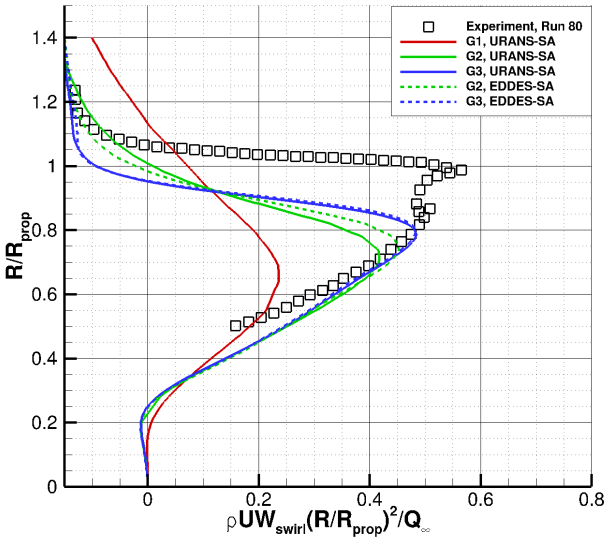

(d) $x = 21.0$ in.

Figure 8: Torque distribution at four stations in the wake of the propeller, $M_\infty = 0.11$, $C_T = 0.40$, $AoA = 0°$

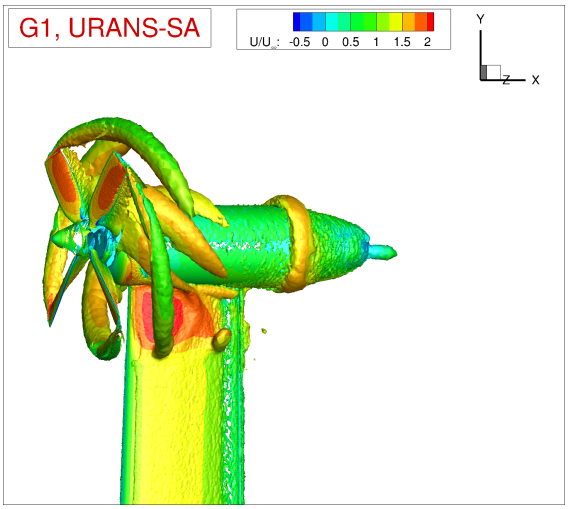

(a) Grid-01 R.

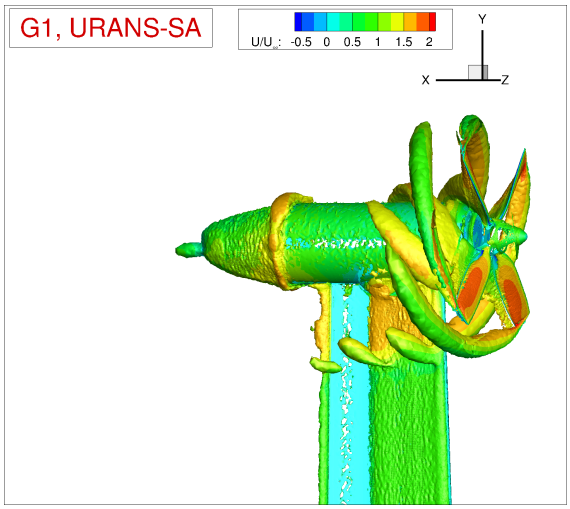

(b) Grid-01 A.

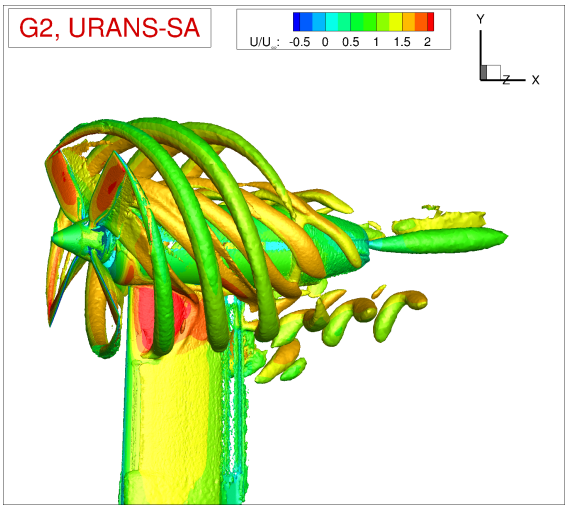

(c) Grid-02 R.

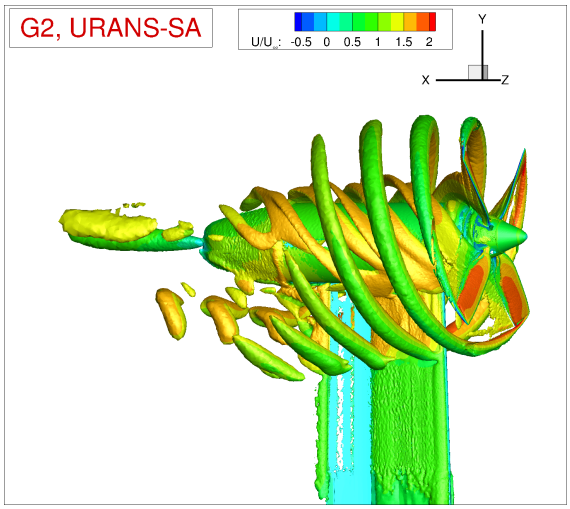

(d) Grid-02 A.

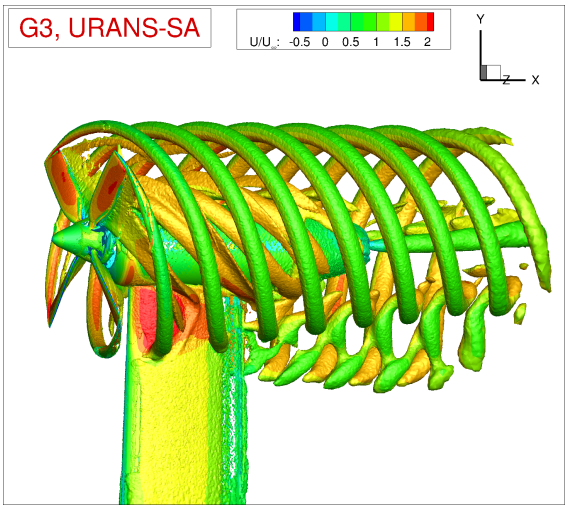

(e) Grid-03 R.

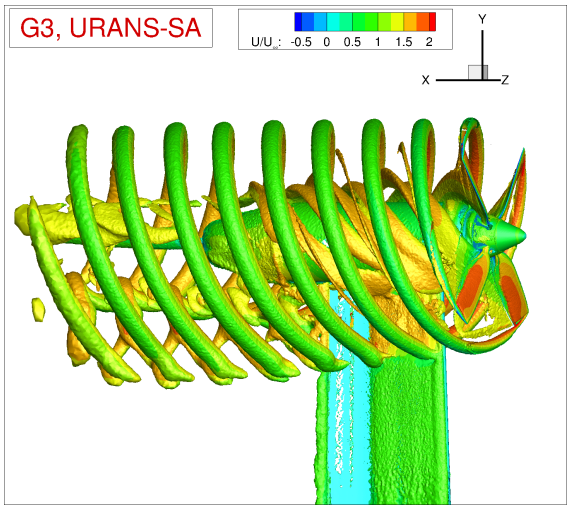

(f) Grid-03 A.

Figure 9: Q-criterion iso-surface colored by the dimensionless streamwise velocity computed by URANS-SA on Grid-01, Grid-02 and Grid-03, $M_\infty = 0.11$, $C_T = 0.40$, $AoA = 0^\circ$

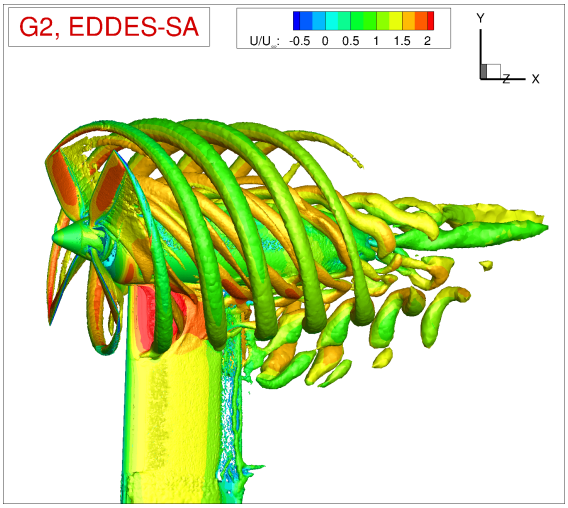

(a) Grid-02 R.

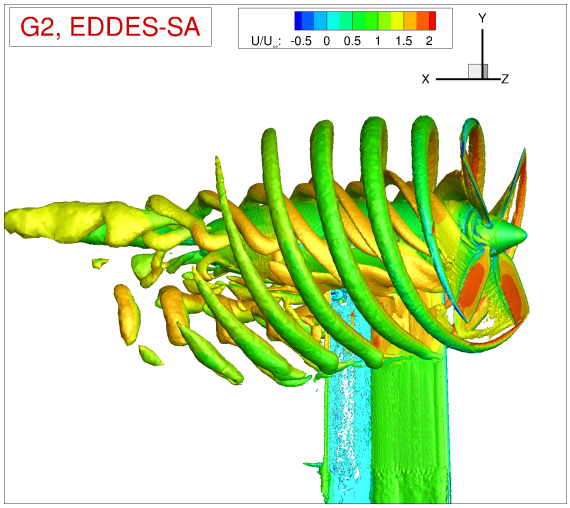

(b) Grid-02 A.

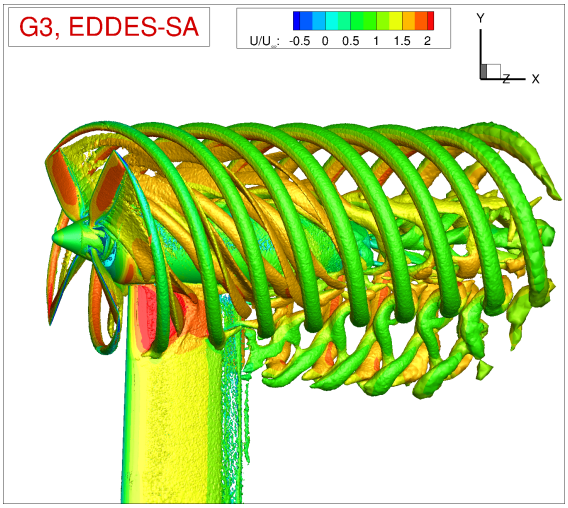

(c) Grid-03 R.

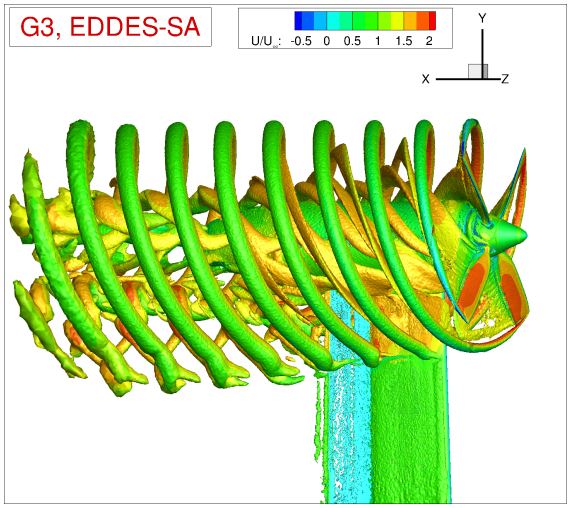

(d) Grid-03 A.

Figure 10: Q-criterion iso-surface colored by the dimensionless streamwise velocity computed by EDDES-SA on Grid-02 and Grid-03, $M_\infty = 0.11$, $C_T = 0.40$, $AoA = 0°$

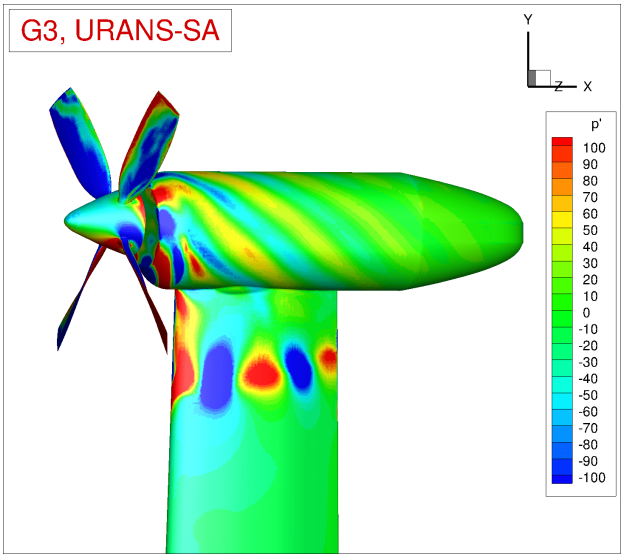

(a) URANS-SA Grid-03 R.

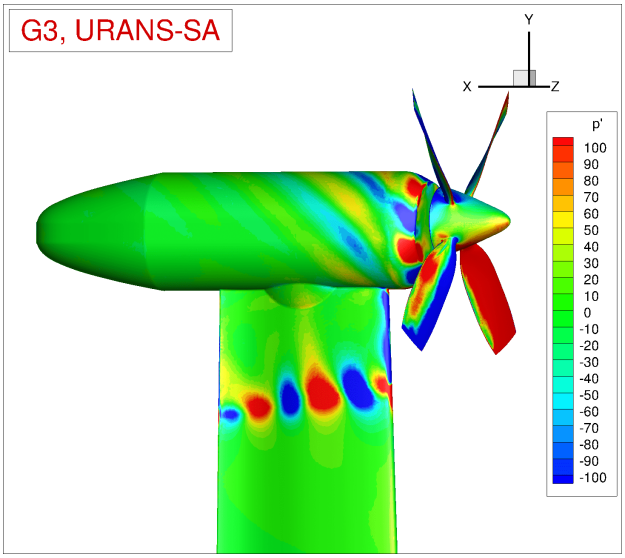

(b) URANS-SA Grid-03 A.

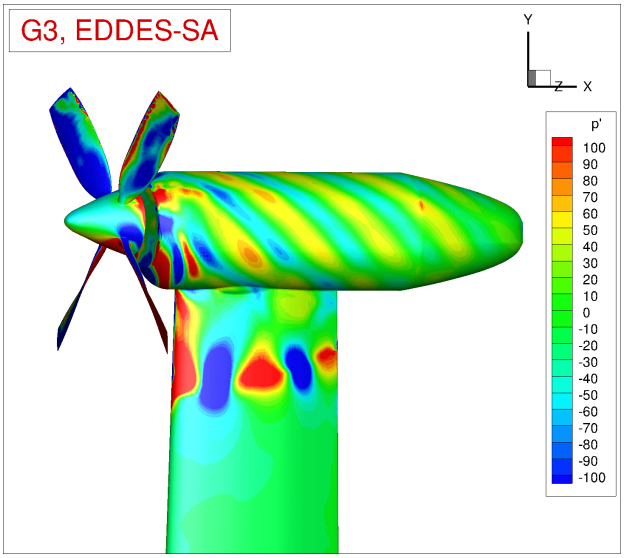

(c) EDDES-SA Grid-03 R.

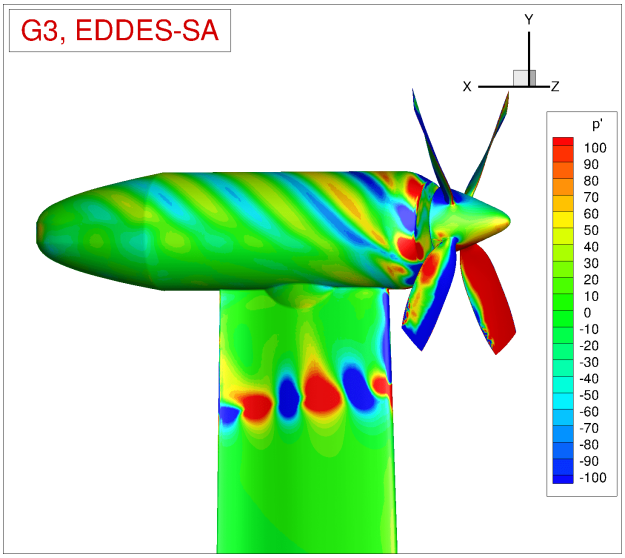

(d) EDDES-SA Grid-03 A.

Figure 11: Instantaneous pressure fluctuation computed by URANS-SA and EDDES-SA on Grid-03, $M_\infty = 0.11$, $C_T = 0.40$, $AoA = 0^\circ$

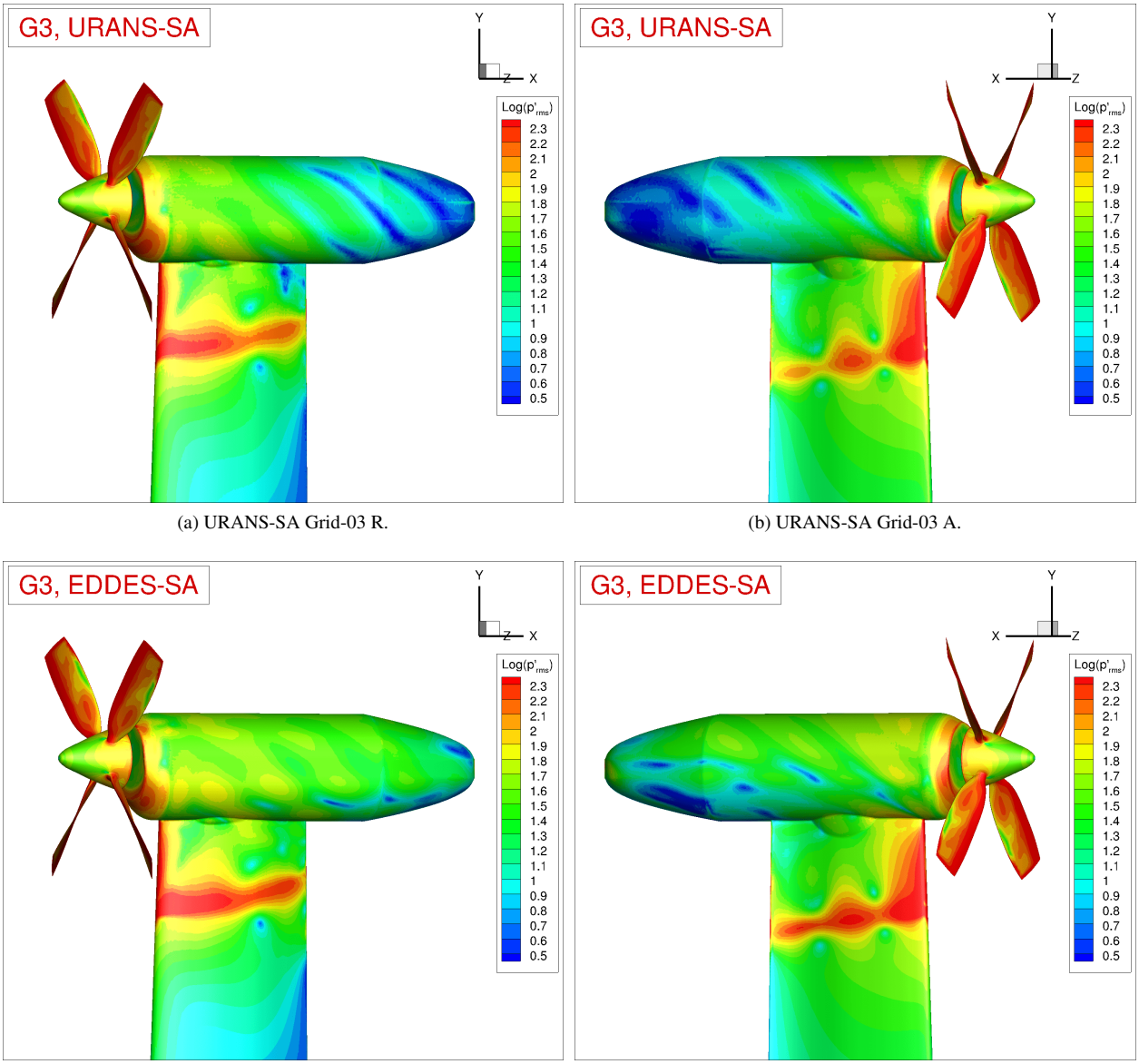

(a) URANS-SA Grid-03 R.

(b) URANS-SA Grid-03 A.

(c) EDDES-SA Grid-03 R.

(d) EDDES-SA Grid-03 A.

Figure 12: The log of root-mean-square of pressure fluctuation computed by URANS-SA and EDDES-SA on Grid-03, $M_\infty = 0.11$, $C_T = 0.40$, $AoA = 0^\circ$

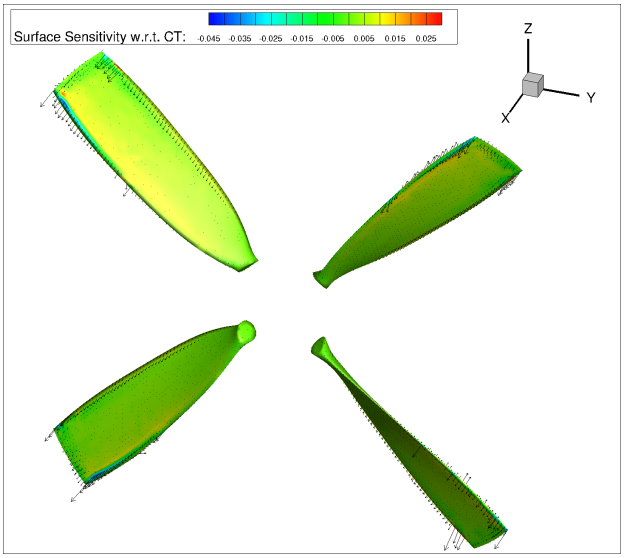

(a) Leeward.

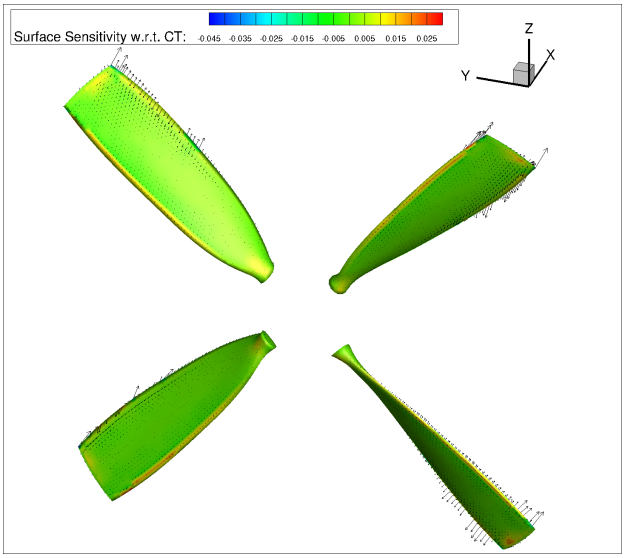

(b) Windward.

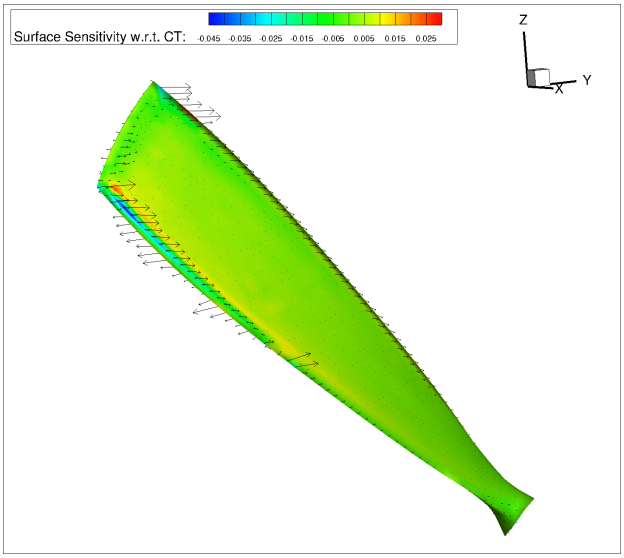

(c) Leeward Single Blade.

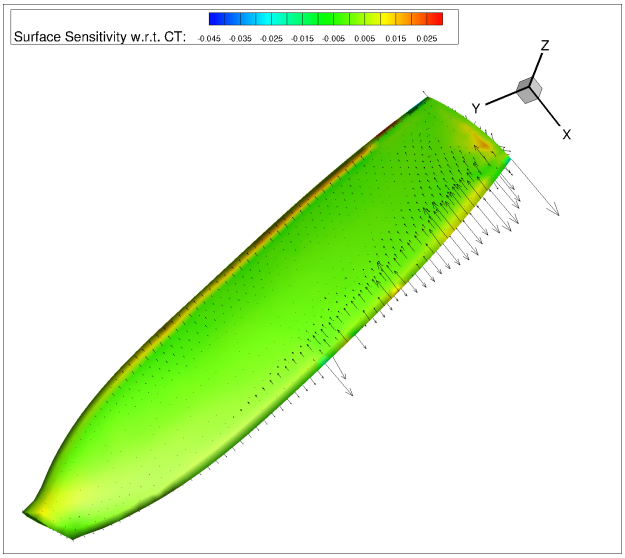

(d) Windward Single Blade.

Figure 13: Surface sensitivity with respect to time-averaged thrust coefficient ($J = \bar{C}_T$), $M_\infty = 0.11$, $C_T = 0.40$, $AoA = 0^\circ$